ADVANCED MATERIALS INTERFACES
Open Access
www.advmatinterfaces.de

Interface Dependent Coexistence of Two-Dimensional Electron and Hole Gases in Mn-doped InAs/GaSb

Logan Riney, Seul-Ki Bac, Maksym Zhukovskyi, Tatyana Orlova, Shelby S. Fields, Jiashu Wang, Tommy Kotte, David Graf, Steven P. Bennett, Xinyu Liu, and Badih A. Assaf**

The interface of common III-V semiconductors InAs and GaSb can be utilized to realize a two-dimensional (2D) topological insulator state. The 2D electronic gas at this interface can yield Hall quantization from coexisting electrons and holes. This anomaly is a determining factor in the fundamental origin of the topological state in InAs/GaSb. Here, the coexistence of electrons and holes in InAs/GaSb is tied to the chemical sharpness of the interface. Magnetotransport, in samples of Mn-doped InAs/GaSb cleaved from wafers grown at a spatially inhomogeneous substrate temperature, is studied. It is reported that the observation of quantum oscillations and a quantized Hall effect whose behavior, exhibiting coexisting electrons and holes, is tuned by this spatial nonuniformity. Through transmission electron microscopy measurements, it is additionally found that samples that host this co-existence exhibit a chemical intermixing between group III and group V atoms that extends over a larger thickness about the interface. The issue of intermixing at the interface is systematically overlooked in electronic transport studies of topological InAs/GaSb. These findings address this gap in knowledge and shed important light on the origin of the anomalous behavior of quantum oscillations seen in this 2D topological insulator.

1. Introduction

Interfaces between unlike materials enable unexpected new physics and important functionalities. Interfaces of unlike insulators have been exploited to generate unconventional two-dimensional (2D) electron gases.[1–5] Interfaces of semiconductors InAs and GaSb have been exploited to engineer infrared devices operating at low wavelengths that cannot be attained in bulk crystals.[6–8] More recently, semiconductor interfaces have also been exploited to generate a topological insulating state[9–16]. Oftentimes, the chemistry and defect structure at an interface plays a critical role in the physics that is ultimately generated,[15,17–19] but this role remains under-appreciated and, in many instances, overlooked.

The band alignment diagram of InAs and GaSb is shown in **Figure 1a**. The valence band of GaSb lies ≈150meV above the conduction of InAs yielding a type-II band alignment. In superlattices, this band alignment enables an engineering of the band gap, that has been exploited to design infrared devices operating at wavelengths not attainable in bulk III-V semiconductors. In 2D and for a specific range of thicknesses,[3,9,10,20] the highest hole subband at the InAs/GaSb interface lies above the lowest electron subband. These two energy bands hybridize causing an inverted energy gap which generates helical topological edge modes. Several aspects of band-inverted of InAs/GaSb remain under study. For instance, the nature of the energy

L. Riney, S.-K. Bac, J. Wang, X. Liu, B. A. Assaf
Department of Physics and Astronomy
University of Notre Dame
Notre Dame, IN 46556, USA
E-mail: xliu2@nd.edu; bassaf@nd.edu

M. Zhukovskyi, T. Orlova
Notre Dame Integrated Imaging Facility
University of Notre Dame
Notre Dame, IN 46556, USA

The ORCID identification number(s) for the author(s) of this article can be found under https://doi.org/10.1002/admi.202400630

DOI: 10.1002/admi.202400630

S. S. Fields, S. P. Bennett
Materials Science and Technology Division
U.S. Naval Research Laboratory
Washington, DC 20375, USA

T. Kotte
Dresden High Magnetic Field Laboratory (HLD-EMFL)
Helmholtz-Zentrum Dresden-Rossendorf (HZDR)
01328 Dresden, Germany

D. Graf
National High Magnetic Field Laboratory
Florida State University
Tallahassee, FL 32310, USA

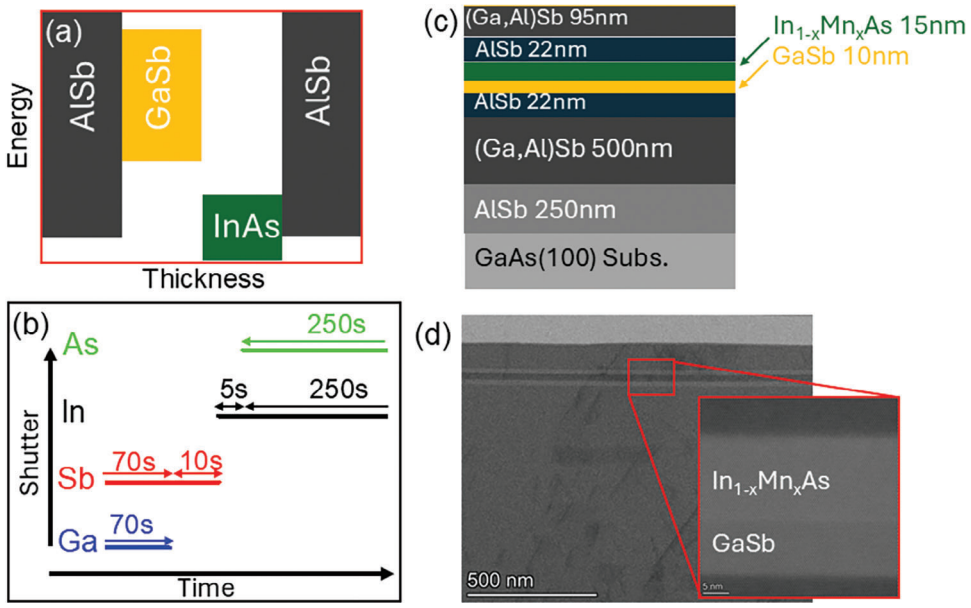

Figure 1. a) Broken-gap (type-II) band alignment at the InAs/GaSb interface. b) MBE shutter sequence employed to obtain an In-Sb interface between InAs and GaSb. c) Structure of the investigated samples. d) Transmission electron microscopy image of the (In,Mn)As/GaSb heterostructure with inset showing a zoom in on the active region.

gap in this system remains controversial.[11] While standard non-interacting models indicate that the gap is a single-particle gap, many experiments have suggested that it has an excitonic nature.[11,21–23] This excitonic nature has been recently inferred from the observation of quantum oscillations at charge neutrality and the coexistence of electrons and holes in quantum oscillations. But even as long as four decades ago, these observables in InAs/GaSb raised the question of whether single particle models—generally used to model device functionality—are sufficient to describe the physics observed experimentally in this system.[24] The chemistry of the interface and its impact on the electronic structure is also critical to study from a fundamental standpoint,[25,26] but it is systematically overlooked in magnetotransport studies.

Using quantum oscillations at high magnetic fields in Mn-doped InAs/GaSb, we have observed coexisting 2D electron and hole gases (2DEG and 2DHG respectively) with a high electron density. The inclusion of Mn is motivated by its role as an acceptor that tunes the Fermi level of this system.[27] Surprisingly, the coexistence of a 2DEG and a 2DHG is reproducible but is not consistently observed in every piece of the same wafer. The 2DHG is also detected both in the Hall effect in pieces cleaved from the middle of the wafer, but is absent in pieces cleaved from the edge. We combine this systematic magnetotransport study with high-resolution transmission electron microscopy (TEM) measurements enabled by state-of-the-art aberration correction. We correlate the presence of the hole gas to the quality of the InAs-GaSb interface. From our experimental findings, we hypothesize that an intermixed layer at the InAs/GaSb interface manifesting in TEM is responsible for the manifestation of the coexisting 2DHG and 2DEG. This layer can alter the energy separation between the lowest electron and highest hole state, and can act as a hole trap. Our work demonstrates the critical role of interface chemistry in this material, important to control, to both achieve reliable infrared sensors and topological states in this system.

2. Results and Discussion

InAs/GaSb doped with Mn are grown by molecular beam epitaxy (MBE) following a process described in ref.[27]. During the growth of the InAs/GaSb bilayer, we intentionally terminate the GaSb layer with InSb following the shutter sequence shown in Figure 1b. The sample structure is shown in Figure 1c. We focus our attention on samples cleaved from two wafers grown with a Mn cell temperature of 600 and 615 °C. The wafers are labeled by the Mn cell temperature (Wafer-600 and Wafer-615 respectively). The Mn content is estimated to be 0.2% for wafer 615 and was undetectable for wafer 600 (<0.1%). The determination of the Mn content is shown in Section S2 (Supporting Information).

Magnetotransport measurements are carried out at high magnetic fields using a pulsed field setup located at the Dresden High Magnetic Field Laboratory (HLD) capable of field up to 70T, a DC field setup located at the National High Magnetic Field Lab (NHMFL) in Tallahassee capable of up to 31T, and as well as an MPMS-5 System onsite capable of 7T. The temperature dependence of the Hall resistance, the magnetoresistance and of quantum oscillations is studied down to 1.5K. X-ray photoemission spectroscopy (XPS) measurements are carried out at the Naval Research Laboratory using a Thermo Fisher Scientific Nexsa XPS equipped with an Al Kα source, and fitted using Thermo Fisher Avantage analysis software. Cross-sectional transmission electron microscopy images were acquired using a double-tilt holder and probe-corrected Spectra 30–300 transmission electron microscope (Thermo Fisher Scientific, USA) equipped with a field emission gun. The thicknesses shown in Figure 1c are confirmed by transmission electron microscopy measurements (Figure 1d).

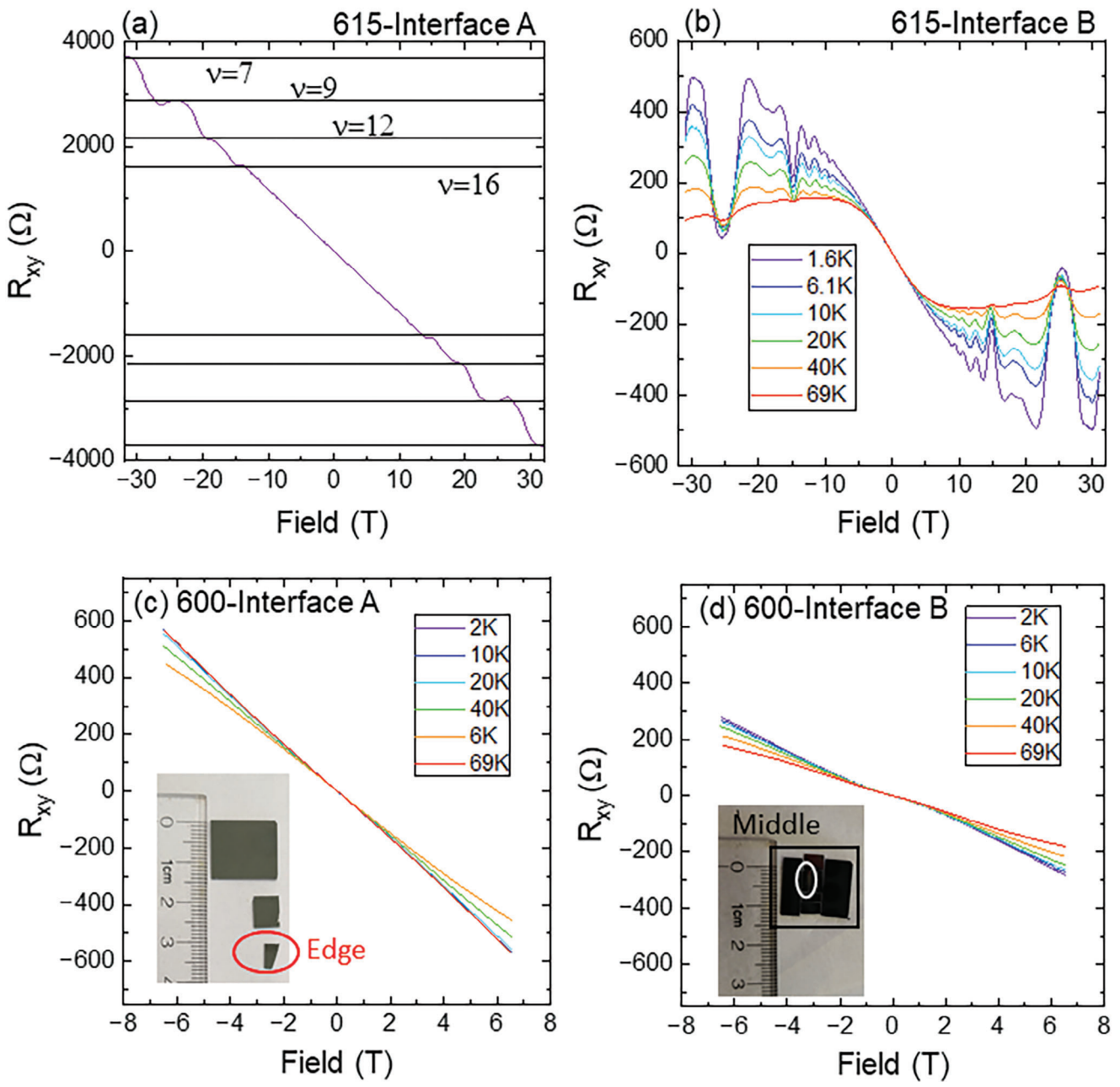

Figure 2. a) Quantized Hall resistance measured on sample labeled Interface A. b) Hall resistance measured on a sample labeled Interface B. b) Both samples are cleaved from Wafer 615. c) Hall resistance measured in a sample cleaved from the edge of Wafer 600 exhibiting a large linear behavior as seen for interface A. d) Hall resistance cleaved from the middle of Wafer 600, exhibiting a weaker Hall effect as seen for Interface B.

The Hall resistance measured in two pieces cleaved from Wafer-615 is shown in **Figure** 2a,b. In one instance the Hall effect is linear at low field and exhibits a clear quantization of the Hall resistance at high magnetic field, reaching a filling factor ν of 7 by 30T (Figure 2a). In another case (Figure 2b), the Hall resistance exhibits a weaker low field slope and quantum oscillations but is not quantized. Both measurements yield a negative slope at low magnetic field indicating n-doping, but in Figure 2b a downturn is observed implying the coexistence of electrons and holes. In the remainder of this work, we refer to the sample exhibiting a quantized Hall resistance as Interface A and the sample exhibiting a non-linear Hall resistance as Interface B. This spatial dependence of the Hall resistance and the carrier density is confirmed for Wafer-600 (Figure 2(c,d)). There, we find a suppressed Hall resistance as seen for Interface B in pieces cleaved from the middle of the wafer, while the edge of the wafer exhibits a large Hall slope consistent with behavior seen for Interface A.

We study the temperature dependence of the magnetoresistance to determine the origin of the Fermi pocket responsible for the behavior seen in the Hall effect. We focus on Wafer-615.

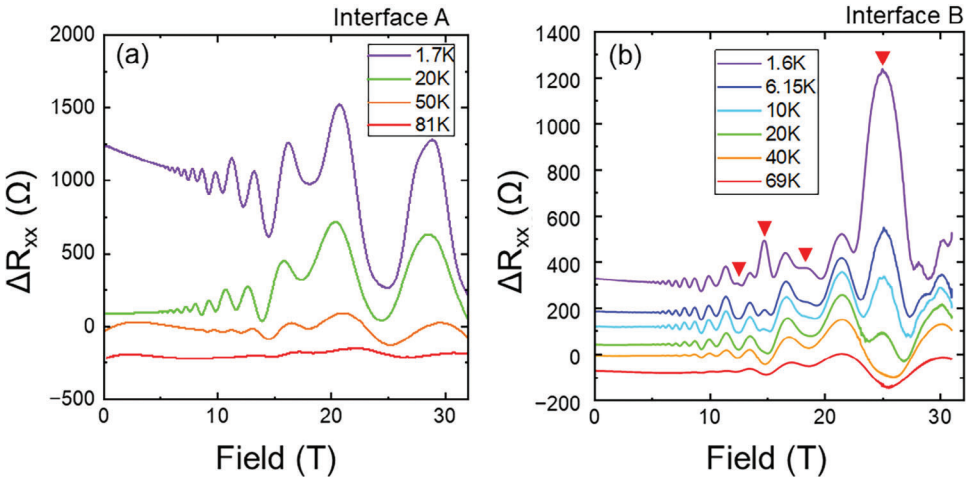

Figure 3. Quantum oscillations in the magnetoresistance measured on Interface A (a) and Interface B (b) samples from Wafer-615. The red triangles label anomalous oscillations that decay quickly with increasing temperature.

Interface A exhibits Shubnikov-de-Haas (SdH) oscillations expected for a high mobility 2D system, as shown in **Figure 3**a. The amplitude of the oscillations drops with increasing temperature. The SdH oscillations yield two frequencies as we have shown in our previous work.[27] They are due to partial occupancy of two electron subbands. Interface B exhibits a very different type of oscillation as shown in Figure 3b. At high temperature (40K and above), the oscillations seen in Interface B are identical to those seen in Interface A. However, as we lower the temperature, additional maxima – labeled by red arrows – emerge and gain in amplitude. We shall next show that the additional maxima are due to a hole gas. The Fourier analysis of the quantum oscillations and its comparison with the Hall effect is shown in Section S1 (Supporting Information).

The changing amplitude of the oscillations ΔR_{xx} as a function of temperature is then extracted and fitted with the Lifshitz-Kosevich (LK) formula.

$$\Delta R_{xx} \propto \frac{\chi(B,T)}{\sinh \chi(B,T)} \tag{1}$$

where

$$\chi(B,T) = \frac{2\pi^2 m^* k_B T}{\hbar e B} \tag{2}$$

Here, m^* is the effective mass, B is the magnetic field at which an oscillation maximum occurs. T is the temperature, k_B, e, and $\hbar$ have their usual meaning. The decaying amplitude of oscillation maxima extracted for interface A between 8T and 31T is shown in **Figure** 4a. The LK formula yields excellent fits to the decay, yielding an effective mass that increases monotonically with increasing magnetic field from $0.058\pm0.001 m_0$ at 8.6T to $0.17\pm0.01 m_0$ at 28T. The trend is plotted in Figure 4b. The masses recovered at low magnetic field for interface A agree with the mass extract from cyclotron resonance measurements performed in our previous work.[27] The value of m^* is also typical of the effective mass of electrons found in InAs/GaSb and InAs leading us to attribute the SdH oscillations to electrons, consistent with the normal Hall effect seen at low field in Figure 2a.

The LK analysis of Interface B oscillations unveils a different situation, manifesting a coexistence of electrons and heavy holes (HH). Figure 4c plots the quickly decaying oscillation amplitude for two anomalous maxima seen at 14.74T and 25.2T. A curve fit using the LK formula up to 4.2K yields a mass exceeding $0.3 m_0$ for both oscillation maxima. Such a high effective mass is characteristic of HH in III-V semiconductors. We highlight that the LK formula does not yield a good fit to the data when it is performed over the entire temperature range between 1.5K and 70K (solid line in Figure 4c) and likely overestimates the mass ($>0.6 m_0$). From that we conclude that the LK formula does not represent the physical picture of the temperature dependence of Interface B for HH. Figure 4d plots the decaying oscillation amplitude for the remaining oscillations seen in the data for Interface B. The LK formula yielded an excellent fit up to 9.9T, again yielding effective masses typical of electrons ($\approx 0.05 m_0$). At higher magnetic fields, the decaying trend of the LK equation fails to describe the temperature dependence seen below 6K for Interface B, as oscillations get weaker when temperature drops from 6K to 1.5K. This anomaly is only seen at magnetic fields where oscillations attributed to electrons occur near those attributed to HH.

Figure 4b summarizes the magnetic field dependence of the effective mass for Interface B. At low magnetic fields, the effective mass agrees with what is found for Interface A. At higher fields, above 10T, oscillations from HH emerge. At the same magnetic field, the amplitude trend is no longer properly described by the LK formula for electrons and yields an underestimate. This explains the divergence in m^*/m_0 seen when comparing Interface B to Interface A above 10T.

We note that the anomalous oscillations seen for Interface B and the normal pattern seen for Interface A are reproduced in the different pieces cleaved from the same wafer. We therefore rule out the possibility that uncontrolled factors in the experiments yield these differences. In Section S1 (Supporting Information), we also successfully fit the field dependence of R_{xy} from Figure 2b, using the carrier densities extracted for electrons and holes from the SdH frequency. This agreement validates the fact that the emerging 2DHG detected in Figure 3b alters the behavior of the Hall effect shown in Figure 2.

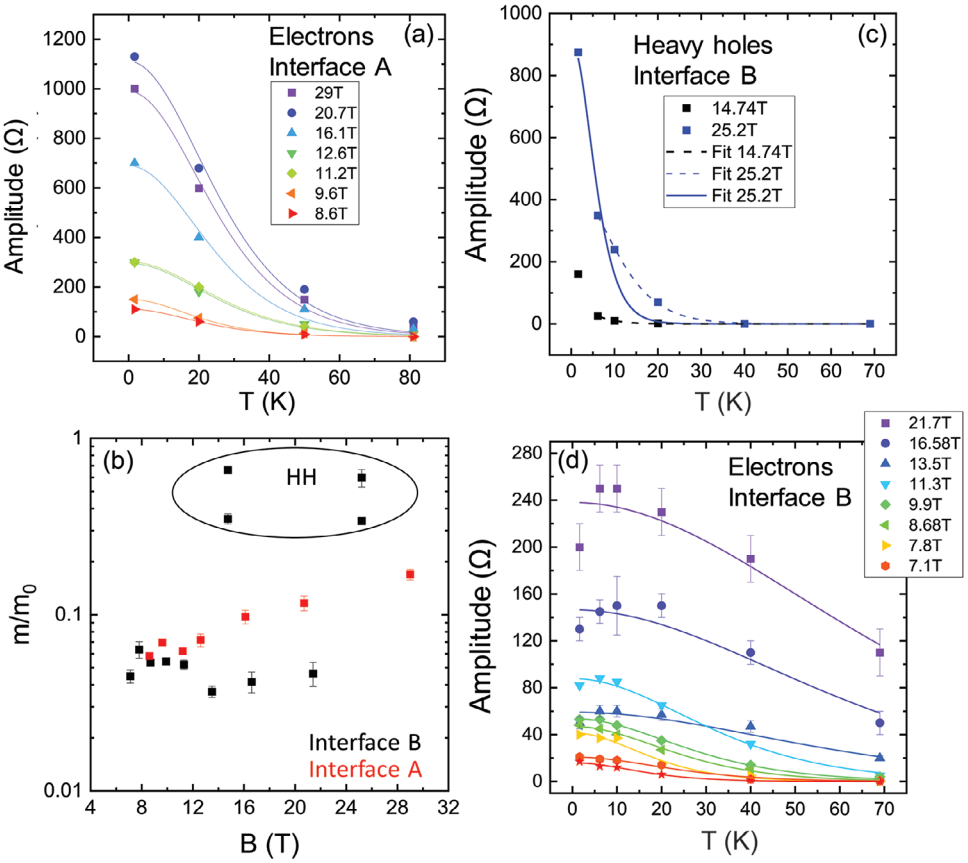

Figure 4. Temperature dependence of the oscillation maxima (points) fitted with the LK relation (solid lines, Equation (1)). a) Analysis of the oscillations measured in Interface A. b) Effective mass for both interfaces (A in red and B in black) as a function of the magnetic field at which each oscillation maximum occurs. The circle labels the heavier effective masses, expected to be those of HH. The two values represent two fitting schemes that either exclude or include the data at 1.6K. c) Analysis of the anomalous and d) normal oscillations seen in interface B respectively. The dashed lines in (c) exclude points at 1.6K. The error bars in (d) are due to uncertainty in the background determination.

To further characterize the structure and chemistry of the interface, we performed transmission electron microscopy measurements on pieces of Wafer-615 after they were utilized for magnetotransport and labeled according to their behavior at high magnetic field (Interface A vs B). Scanning TEM (STEM) images were acquired using Panther STEM detector (Thermo Fisher Scientific, USA) in high-angle, annular dark field mode (HAADF) and bright field mode (BF). Low magnification BF images taken respectively on a piece cleaved from an Interface-A and an Interface-B sample are shown in **Figure 5**a,b. There is no noticeable difference in thickness of the InAs and GaSb layers between the two sample types.

High magnification measurements are then obtained on randomly chosen regions along the interface of the samples. Two zoomed-in HAADF images collected on Interface A are shown Figure 5c,d. Two collected for Interface B are shown in Figure 5e,f. The HAADF signal is known to be sensitive to atomic number and is thus a good characterization tool to study the sharpness of interfaces. The films are oriented with the (001) direction pointing along the vertical and the [1–10] direction pointing in the plane of the page. The (110) projection of the zincblende unit cell allows us to identify individual atomic columns in the images. On the bottom end of the image, the larger bright circles correspond to Sb columns and the smaller ones to Ga columns. At the top end, the larger bright circles correspond to In columns and the smaller ones to As columns. The images reveal the consistent formation of an In-Sb interface. Additional TEM images are included in Section S3 (Supporting Information).

To determine the quality of the interface at a scale larger than an individual linecut, we extract the signal intensity by taking linecuts of the TEM image along each individual columns identified by arrows in Figure 5c,e. Two equivalent offset layers of atoms characteristic of the zincblende structure are averaged separately. We plot the average HAADF intensity as a function of the vertical pixel position in **Figure 6**a,b for Interface A and Interface B, respectively. The linecuts exhibit a set of double peaks that can be identified as the group III and group V atomic columns. Starting from the left, the weaker peak presents As columns and the stronger one represents In. The relative intensity is swapped after we cross the interface into the GaSb layer, where the weak peak can be identified as the Ga atomic column and the stronger peak is the Sb atomic column.

To restrict our analysis to the local features of each image, we extract the difference in intensity between the group III and group V atomic columns for each layer ($\Delta_{III-V} = I_{III} - I_V$).

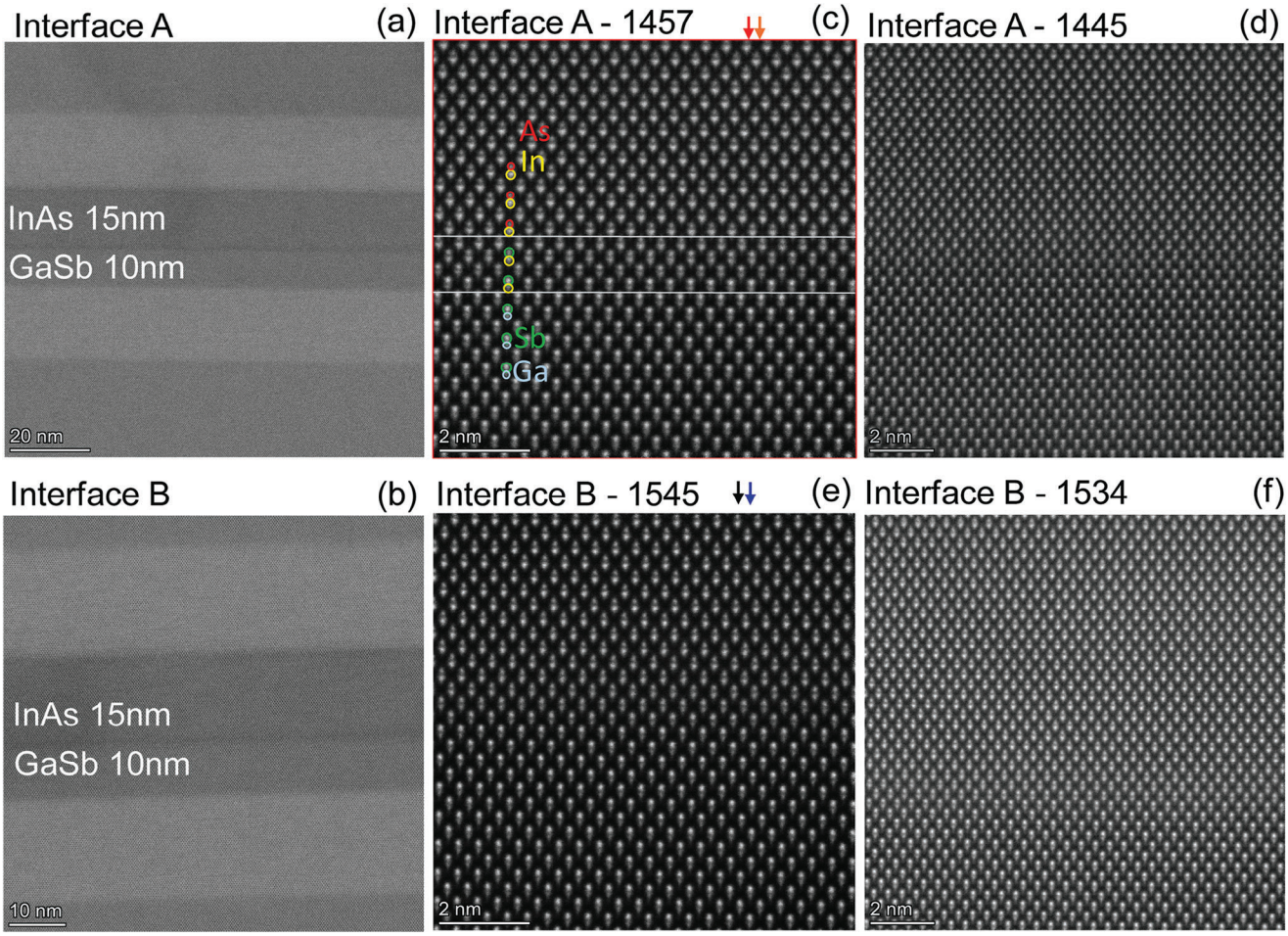

Figure 5. Low magnification images of Interface A (a) and Interface B (b). High magnification images of Interface A (c,d) and Interface B (e,f). The numbers labeling the images (1457, 1445, 1545, 1534) are identifiers of each individual image, needed for the analysis presented in Figure 5. The scale bar in (c–f) is 2 nm.

Δ_{III-V} is plotted versus layer number in Figure 6c,d. The InAs (GaSb) layer yields a positive (negative) plateau, while the interface is the region where Δ_{III-V} changes sign. We define the interface following two schemes. In the first, we define the interface as data points for which Δ_{III-V} falls two standard deviations outside the plateau. The interface highlighted in gray in Figure 6c,d includes points that satisfy this condition. We find an interface thickness of four layers or six layers from two images shown for Interface A. And we find an interface thickness of six layers or eight layers from two images shown for Interface B.

A more complete statistical study following the procedures described in Figure 6, reveals that there is a stronger intermixing between different atomic species in Interface B. We analyze additional datasets beyond the four extracted from the four TEM images shown in Figure 5 in Section S3 (Supporting Information). The results from all analyzed datasets are plotted in **Figure 7**. The mean interface thickness can be found by averaging the thickness obtained from each data. We find a thickness of 4.2 ± 0.6 *monolayers* for interface A and 5.3 ± 0.7 *monolayers* for interface B (black points in Figure 7). An important parameter in our statistics is the cutoff chosen to define the interface in Figure 6c,d. If we reduce this cutoff to one standard deviation about the plateau, we find a mean thickness of 4.6 ± 0.5 *monolayers* for interface A 6.2 ± 0.6 *monolayers* for Interface B (blue points in Figure 7). Details from this analysis are shown in Section S3 (Supporting Information). We conclude that depending on the parameters of the analysis, Interface B appears 1 to 2 monolayers thicker than Interface A. Since TEM probes atomic columns along the cross-section, we conclude that the larger span revealed for Interface B is evidence of a stronger intermixing between the two group III (and V) elements.

According to a prior work, interfacial intermixing is not uncommon in InAs/GaSb.[28–32] Its impact on the electronic structure was even theoretically studied in InAs/GaSb superlattices[25,26,33–35] and was utilized to explain why the electron to heavy-hole optical transition depended on growth temperature.[36] A theoretical study[25] highlighted that the HH levels are strongly localized in InSb interfacial layers, and their energy is impacted by the quality of the interface.[33,34]

It is important to raise the question of whether a difference of one or two monolayer between the two interface types is enough to account for our observations. Rodriguez et al.[37]

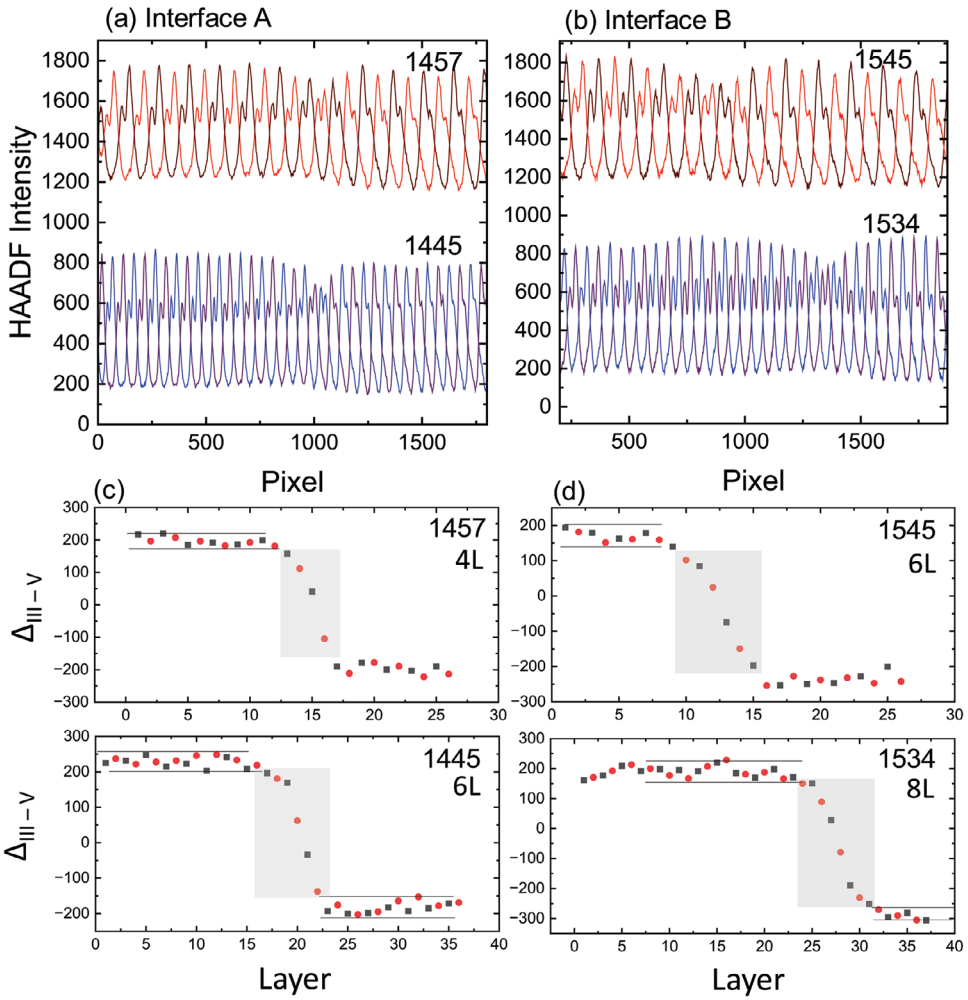

Figure 6. Average linecut extracted by averaging all linecuts extracted from a) Interface A – images number 1457 (red, dark red) and 1445 (blue, purple) and b) Interface B – images number 1545 (red, dark red) and 1534 (blue, purple). Two linecuts for each image represent the two zincblende III-V monolayers stacked along (001). c,d) Difference between the intensity of the group-III atomic column and the group V atomic column for interface A and B, respectively. The solid lines represent an interval of two standard deviations about the average intensity of the plateau regions representing the InAs and GaSb layers. The shaded regions highlight the interface. The interface is defined as the region where $I_{III} - I_V$ falls 2σ outside the average intensity of the plateau.

have studied this systematically by varying the thickness of the intermediate InSb layer and showed that an increase in the InSb layer thickness beyond 1ML (for a 10ML/10ML InAs/GaSb superlattice) impacts the surface roughness, the photoluminescence intensity, and emission wavelength.

Thus, the electronic behavior seen in wafers 615-Interface B and wafer 600-Interface B can be correlated to a thicker intermixing layer at the interface between InAs/GaSb. This intermixing causes holes possibly originating from native defects in the GaSb layer[38] to be trapped at the interface. The observation of a varying Hall resistance across different parts of Wafer-600 also correlates the differences to small substrate temperature variations across the 2'' inch wafer holder utilized during growth, known to impact sample quality in superlattices.

The InAs/GaSb samples studied here are doped with a dilute amount of Mn. The Mn content is estimated by magnetometry measurements and XPS shown in the supplement. The Mn content in Wafer-615 is found to be comparable in order of magnitude to Wafer-630 (0.13%).[27] The signal from Wafer-600 is below the detection limit.[39] We can, however, rule out that Mn doping is responsible for the coexisting 2DEG and 2DHG revealed here. The dependence of the Hall resistance on spatial location on the wafer seen in Wafer-600, and its reproduction in Wafer-615, despite the high Mn content rules out the role of Mn. Mn does however lower the Fermi level by introducing holes[40,41] that compensate the native n-doping of InAs, as we have shown in our previous work.[27] This explains why Wafer-615 has a lower carrier density than Wafer-600. This is reproduced in both Interface A and Interface B, where a nearly identical electron density is found from low field quantum oscillations.

3. Conclusion

Our study hence shows a correlation between the magneto-transport behavior and the interface characteristics of Mn-doped InAs/GaSb enabled by an inhomogeneous substrate temperature

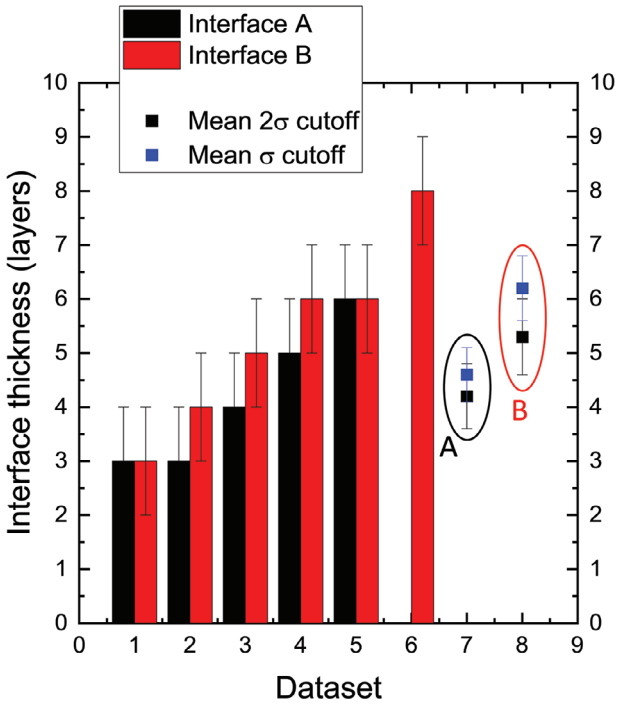

Figure 7. Statistical analysis of the interface thickness done on additional datasets for each sample (black bars: interface A, red bars: interface B). The mean interface thickness (black points) is extracted by averaging the thickness of all studied datasets. The mean interface thickness plotted as blue points represents the average thickness extracted from the $I_{III} - I_V$ plots (c,d) with a cutoff of σ instead of 2σ.

during growth. This finding reveals the critical role of the interface in determining the physics of the InAs/GaSb quantum well system. The problem of defects at this interface has been theoretically and experimentally studied in the past but mostly in the context of infrared devices. It is a highly challenging issue that common models based on the envelope function scheme cannot capture with ease.[42–45] We note that past work has reported the observation of a coexisting 2DEG and 2DHG in InAs/GaSb[11,22,23,46–48] and recent work claimed that this coexistence could be a result of the formation of an exciton state binding an electron to a hole in InAs/GaSb.[11,23] Here our n-type carrier density is close to 5×10^{12} cm^{-2} exceeding what is found in these past studies by at least a factor of 5, yet we still observe coexisting electron and holes. The interpretation relying on exciton condensation is unlikely to be the cause behind our observations, as it will require a large binding energy, given the high Fermi energy. The question of how to account for this coexistence of electrons and holes is an important fundamental question that can impact the physics of the quantum Hall effect, the study of topological insulating behavior in III-Vs and the design of high-performance infrared detectors based on III-V interfaces.

4. Experimental Section

Synthesis: InAs/GaSb doped with Mn were grown by molecular beam epitaxy. A GaAs substrate was first loaded into the MBE and its oxide layer was desorbed by annealing under an As flux. Then, a series of strain-relieving buffer layers was grown as follows: 250 nm AlSb, 500 nm (Al,Ga)Sb, and 22 nm AlSb. This was followed by a 10 nm GaSb well, a 15 nm InAs well, a 22 nm AlSb top barrier, 95 nm (Al,Ga)Sb, and a 2–3 nm GaSb capping layer to prevent the oxidation of Al containing layers. The Mn cell was only open during the growth of the InAs layer. Three samples are studied in this manuscript, Wafer-600, Wafer-615, and Wafer-630, grown with a Mn cell temperature equal to 600 °C, 615 °C, and 630 °C respectively.

Magnetotransport Measurements: Magnetotransport measurements were carried out at high magnetic fields using a pulsed field setup located at the Dresden High Magnetic Field Laboratory (HLD) capable of field up to 70T, a DC field setup located at the NHMFL in Tallahassee capable of up to 31T, and as well as an MPMS-5 System onsite capable of 7T. At HLD the samples are excited using an AC current at a frequency equal to 3.13 kHz. A DC current equal to 10 μA (100 μA) was employed at the NHMFL (onsite).

Transmission Electron Microscopy: Cross-sectional transmission electron microscopy images were acquired using a double-tilt holder and probe-corrected Spectra 30–300 transmission electron microscope (Thermo Fisher Scientific, USA) equipped with a field emission gun.

X-Ray Photoemission Spectroscopy: XPS measurements were carried out at the Naval Research Laboratory using a Thermo Fisher Scientific Nexsa XPS equipped with an Al Kα source, and fitted using Thermo Fisher Avantage analysis software. For each wafer, the sample surface was milled for 15s, and rXPS spectra were recorded after each milling round. This process was repeated until the signal from the bottom (Al,In)Sb buffer was observed.

Supporting Information

Supporting Information is available from the Wiley Online Library or from the author.

Acknowledgements

The authors acknowledge support from NSF-DMR-1905277. BAA and XL also acknolwedge support from NSF-DMR-2313441. A portion of this work was performed at the NHMFL, which is supported by National Science Foundation Cooperative Agreement No. DMR-2128556 and the State of Florida. A part of this work was supported by HLD-HZDR, a member of the European Magnetic Field Laboratory (EMFL). SSF fand SPB are supported by 6.1 Base Funding at the U.S. Naval Research Laboratory in Washington, D.C. We also ackwnoledge support from the Notre Dame Integrated Imaging Facility for TEM measurements.

Conflict of Interest

The authors declare no conflict of interest.

Data Availability Statement

The data that support the findings of this study are available from the corresponding author upon reasonable request.

Keywords

narrow gap semiconductors, quantum Hall effect, topological insulators

Received: July 29, 2024
Revised: September 17, 2024
Published online: October 13, 2024

[1] J. Mannhart, D. G. Schlom, *Science* **2010**, *327*, 1607.
[2] H. Kroemer, *Phys. E (Amsterdam, Neth.)* **2004**, *20*, 196.

[3] M. Altarelli, *Phys. Rev. B* **1983**, *28*, 842.
[4] A. Gozar, G. Logvenov, L. F. Kourkoutis, A. T. Bollinger, L. A. Giannuzzi, D. A. Muller, I. Bozovic, *Nature* **2008**, *455*, 782.
[5] L. Li, C. Richter, J. Mannhart, R. C. Ashoori, *Nat. Phys.* **2011**, *7*, 762.
[6] D. O. Alshahrani, M. Kesaria, E. A. Anyebe, V. Srivastava, D. L. Huffaker, *Adv. Photonics Res.* **2022**, *3*, 2100094.
[7] H. Sakaki, L. L. Chang, R. Ludeke, C. A. Chang, G. A. Sai-Halasz, L. Esaki, *Appl. Phys. Lett.* **1977**, *31*, 211.
[8] A. Rogalski, P. Martyniuk, M. Kopytko, *Appl. Phys. Rev.* **2017**, *4*, 031304.
[9] L. Du, I. Knez, G. Sullivan, R.-R. Du, *Phys. Rev. Lett.* **2015**, *114*, 096802.
[10] M. J. Yang, C. H. Yang, B. R. Bennett, B. V. Shanabrook, *Phys. Rev. Lett.* **1997**, *78*, 4613.
[11] L. Du, X. Li, W. Lou, G. Sullivan, K. Chang, J. Kono, R.-R. Du, *Nat. Commun.* **2017**, *8*, 1971.
[12] Q.-Z. Wang, X. Liu, H.-J. Zhang, N. Samarth, S.-C. Zhang, C.-X. Liu, *Phys. Rev. Lett.* **2014**, *113*, 147201.
[13] F. Couëdo, H. Irie, K. Suzuki, K. Onomitsu, K. Muraki, *Phys. Rev. B* **2016**, *94*, 035301.
[14] M. Karalic, S. Mueller, C. Mittag, K. Pakrouski, Q. Wu, A. A. Soluyanov, M. Troyer, T. Tschirky, W. Wegscheider, K. Ensslin, T. Ihn, *Phys. Rev. B* **2016**, *94*, 241402.
[15] B. Shojaei, A. P. McFadden, M. Pendharkar, J. S. Lee, M. E. Flatté, C. J. Palmstrøm, *Phys. Rev. Mater.* **2018**, *2*, 064603.
[16] Q. Liu, X. Zhang, L. B. Abdalla, A. Zunger, *Adv. Funct. Mater.* **2016**, *26*, 3259.
[17] B. R. Bennett, *Appl. Phys. Lett.* **1998**, *73*, 3736.
[18] L. Tiemann, S. Mueller, Q.-S. Wu, T. Tschirky, K. Ensslin, W. Wegscheider, M. Troyer, A. A. Soluyanov, T. Ihn, *Phys. Rev. B* **2017**, *95*, 115108.
[19] H. Irie, T. Akiho, F. Couëdo, R. Ohana, K. Suzuki, K. Onomitsu, K. Muraki, *Phys. Rev. B* **2020**, *101*, 075433.
[20] S. S. Krishtopenko, S. Ruffenach, F. Gonzalez-Posada, G. Boissier, M. Marcinkiewicz, M. A. Fadeev, A. M. Kadykov, V. V. Rumyantsev, S. V. Morozov, V. I. Gavrilenko, C. Consejo, W. Desrat, B. Jouault, W. Knap, E. Tournié, F. Teppe, *Phys. Rev. B* **2018**, *97*, 245419.
[21] D. I. Pikulin, T. Hyart, *Phys. Rev. Lett.* **2014**, *112*, 176403.
[22] Z. Han, T. Li, L. Zhang, G. Sullivan, R.-R. Du, *Phys. Rev. Lett.* **2019**, *123*, 126803.
[23] D. Xiao, C.-X. Liu, N. Samarth, L.-H. Hu, *Phys. Rev. Lett.* **2019**, *122*, 186802.
[24] G. Bastard, E. E. Mendez, L. L. Chang, L. Esaki, *Phys. Rev. B* **1982**, *26*, 1974.
[25] R. Magri, A. Zunger, *Phys. Rev. B* **2001**, *64*, 081305.
[26] R. Magri, A. Zunger, *Phys. Rev. B* **2002**, *65*, 165302.
[27] L. Riney, J. Bermejo-Ortiz, G. Krizman, S.-K. Bac, J. Wang, M. Zhukovskyi, T. Orlova, L. A. de Vaulchier, Y. Guldner, R. Winkler, J. K. Furdyna, X. Liu, B. A. Assaf, *Phys. Rev. B* **2022**, *105*, 125301.
[28] E. Luna, F. Ishikawa, B. Satpati, J. B. Rodriguez, E. Tournié, A. Trampert, *J. Cryst. Growth* **2009**, *311*, 1739.
[29] K. Mahalingam, K. G. Eyink, G. J. Brown, D. L. Dorsey, C. F. Kisielowski, A. Thust, *Appl. Phys. Lett.* **2006**, *88*, 091904.
[30] E. Luna, B. Satpati, J. B. Rodriguez, A. N. Baranov, E. Tournié, A. Trampert, *Appl. Phys. Lett.* **2010**, *96*, 021904.
[31] J. Steinshnider, M. Weimer, R. Kaspi, G. W. Turner, *Phys. Rev. Lett.* **2000**, *85*, 2953.
[32] J. Steinshnider, J. Harper, M. Weimer, C.-H. Lin, S. S. Pei, D. H. Chow, *Phys. Rev. Lett.* **2000**, *85*, 4562.
[33] X. Chai, R. Guzman, Y. Zhou, Z. Xu, Z. Liang, Y. Zhu, W. Zhou, J. Chen, *ACS Appl. Mater. Interfaces* **2021**, *13*, 38553.
[34] D. Alshahrani, M. Kesaria, J. J. Jiménez, D. Kwan, V. Srivastava, M. Delmas, F. M. Morales, B. Liang, D. Huffaker, *ACS Appl. Mater. Interfaces* **2023**, *15*, 8624.
[35] M. Rygała, K. Ryczko, T. Smołka, D. Kujawa, P. Martyniuk, T. J. Ronningen, S. Krishna, M. Motyka, *Phys. Rev. B* **2021**, *104*, 085410.
[36] M. J. Yang, W. J. Moore, B. R. Bennett, B. V. Shanabrook, J. O. Cross, W. W. Bewley, C. L. Felix, I. Vurgaftman, J. R. Meyer, *J. Appl. Phys.* **1999**, *86*, 1796.
[37] B. Satpati, J. B. Rodriguez, A. Trampert, E. Tournié, A. Joullié, P. Christol, *J. Cryst. Growth* **2007**, *301*, 889.
[38] P. S. Dutta, H. L. Bhat, V. Kumar, *J. Appl. Phys.* **1997**, *81*, 5821.
[39] A. G. Shard, *Surf. Interface Anal.* **2014**, *46*, 175.
[40] J. Mycielski, *Progress in Crystal Growth and Characterization*.
[41] M. Dobrowolska, K. Tivakornsasithorn, X. Liu, J. K. Furdyna, M. Berciu, K. M. Yu, W. Walukiewicz, *Nat. Mater.* **2012**, *11*, 444.
[42] G. Bastard, *Wave Mechanics Applied to Semiconductor Heterostructures (Les éditions de physique)*, Les Ulis, France **1996**.
[43] R. Winkler, *Spin-Orbit Coupling Effects in Two-Dimensional Electron and Hole Systems*, Springer, Berlin **2003**.
[44] T. Andlauer, P. Vogl, *Phys. Rev. B* **2009**, *80*, 035304.
[45] G. Bastard, *Phys. Rev. B* **1982**, *25*, 7584.
[46] E. E. Mendez, L. Esaki, L. L. Chang, *Phys. Rev. Lett.* **1985**, *55*, 2216.
[47] M. Dyksik, M. Motyka, M. Rygała, A. Pfenning, F. Hartmann, R. Weih, L. Worschech, S. Höfling, G. Sęk, *Opt. Appl.* **2021**, *51*, 171.
[48] M. P. Mikhailova, A. N. Titkov, *Semicond. Sci. Technol.* **1994**, *9*, 1279.